FIRST STREET FOUNDATION

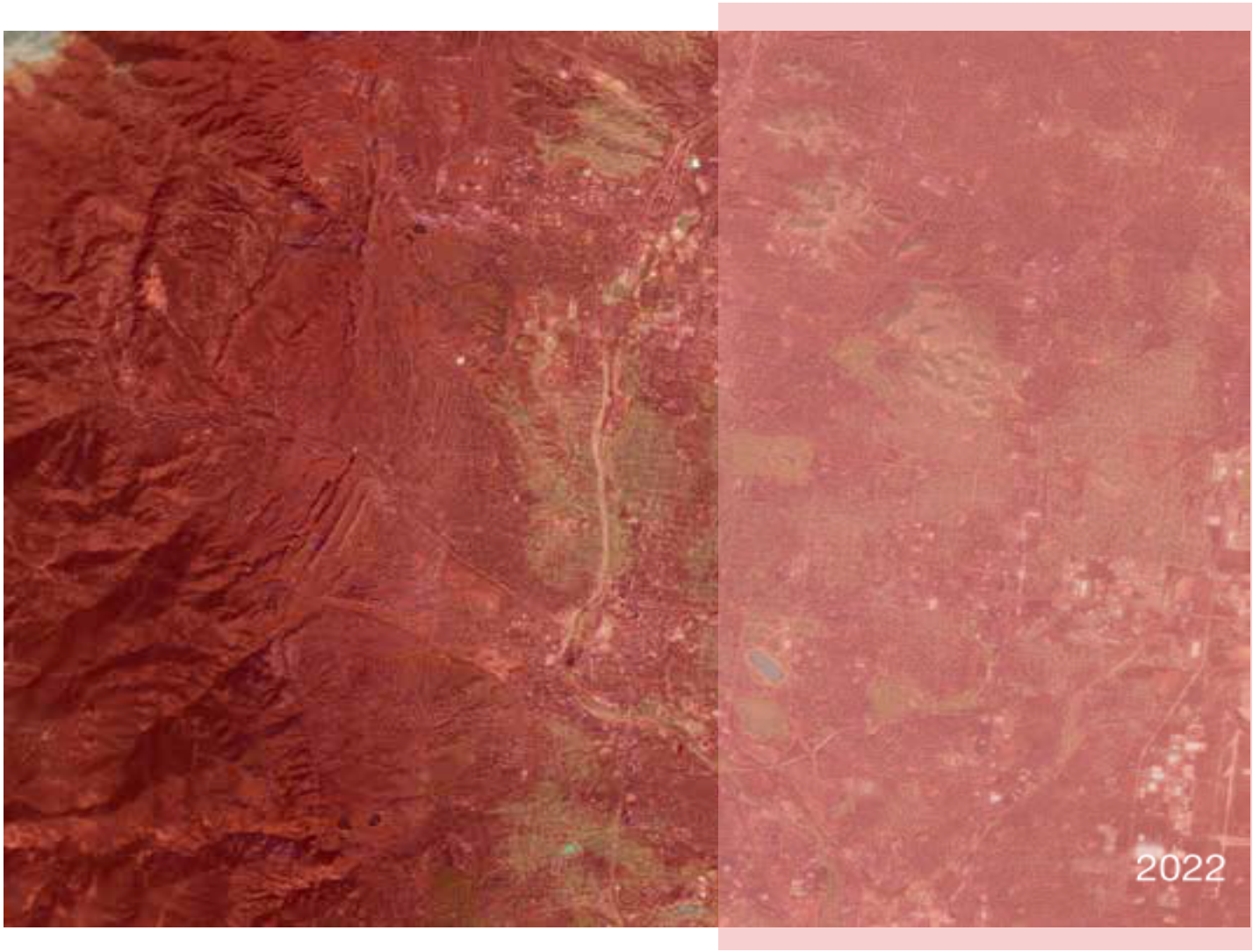

First Street Foundation - Extreme Heat Model

Technical Methodology Document

First Street Foundation - Extreme Heat Model, Technical Methodology

August 15th, 2022

Table of Contents:

Executive Summary:

The United States faces a challenging problem of adapting to extreme heat that is getting worse over time (Rasmussen et al., 2016; Broadbent et al., 2020; Meehl & Tebaldi, 2004). Conservative estimates show temperatures across the United States increasing by a minimum of 2.5°F over the next 30 years (Fourth National Climate Assessment, 2018). Since warmer air has a higher capacity to hold water, increasing evaporation will result in more humid conditions, compounding effects by worsening heat indexes and making health impacts more likely. Illustrating the importance of understanding extreme heat, the U.S. federal government supported the creation of the National Integrated Heat Health Information System (see Heat.gov), published in July 2022, to provide a unified source of information aimed at reducing the health, economic, and infrastructural impacts of extreme heat. The increase in extreme heat conditions are a cause for widespread concern, impacting everything from personal health risk, electricity costs associated with increased air conditioning usage, physical infrastructure, and even safe operation of public transport. While heat patterns are not changing uniformly across the country due to diverse landscapes, vegetation, and urbanization, the ubiquity of climatic changes on temperature and humidity creates a need to ensure that all individuals and communities have access to estimates of their extreme heat risk.

Following the open science approach taken by the nonprofit First Street Foundation for climate-adjusted flood and wildfire risk (Armal et al. 2020; Bates et al. 2021; Kearns et al. 2020), a new analysis was undertaken that would estimate the extreme heat exposure at a property-by-property scale across the United States. The technical documentation for the methodology used by the First Street Foundation Extreme Heat Model (hereafter, FSF-EHM) to compute estimates of the 30-year, climate-adjusted aggregate heat hazard for the contiguous United States at 30 meter horizontal resolution is presented.

The FSF-EHM utilizes several existing methods from the heat science community combined with scalable computational techniques and satellite imagery to produce new high-resolution heat hazards across the contiguous United States (CONUS). U.S. Federal Open Data sources support the production of a high resolution extreme heat product that allows individuals, communities, businesses, and governments to better understand and prepare for their heat risks both today and 30 years into the future. Satellite land surface temperature measurements from Landsat 8 are calibrated to surface air temperature measurements from NOAA climate-quality weather stations to model hyper-local temperature variations. Daily time series of surface temperatures and humidity at 4km resolution are used to produce heat hazards representative of 2023 and 2053 conditions corresponding to IPCC CMIP5 RCP4.5 model ensemble predictions. Together, these components support the assessment of multiple heat hazards including heat waves, dangerously hot days, and days above locally hot thresholds—all important factors in characterizing extreme heat. The heat risk product resulting from this model has been named “Heat Factor” as part of a wider “Risk Factor” information platform provided by the First Street Foundation for free, public use under noncommercial license terms (see riskfactor.com).

The results indicate that the incidence of extreme heat is growing across the country, both in absolute and relative terms. Risk analysis requires consideration of characteristics such as probability and consequences, thus including those events which have low probabilities but high consequences (Garrick & Kaplan, 1981). In absolute terms, the incidence of heat that exceeds the threshold of the National Weather Service's (NWS) highest category for heat, called "Extreme Danger" (Heat Index above 125°F) is expected to impact about 8 million people this year (the estimated populations in counties which have at least one property that is likely to experience a day at or above the 125°F Heat Index), increasing to about 107 million people in 2053, an increase of approximately 13 times in 30 years, holding population counts and patterns constant. This increase in "Extreme Danger Days" is concentrated in the middle of the country, in areas where there are no coastal influences which may help mitigate these extreme temperatures. This zone, termed here the "Extreme Heat Belt," stretches from the Northern border of Texas and Louisiana north through Iowa, Indiana, and Illinois, and demonstrates that many locations likely to bear the brunt of increases in extreme danger over the next 30 years are concentrated inland and in the industrial Midwest, and not necessarily in the Deep South or West. Beyond the incidence of Extreme Danger Days, all areas across the country are expected to experience hotter local temperatures. These increases in local temperatures result in significant implications for communities that are not acclimated to warmer weather relative to their normal climate. This reality suggests that a 10% temperature increase in Maine can be as dangerous as a 10% increase in Texas, even as the absolute temperature increase in Texas is much higher. "Local Hot Days" - defined relative to specific localities, such as states, neighborhoods, or communities - are increasing in frequency across the country, with one significant implication being that a community can expect its 7 hottest days (determined by the 98th percentile heat index value) in the current environment to occur up to 30+ days in 2053. Interestingly, exposure to Consecutive Local Hot Days is most likely to occur in West Coast states, while states in the Midwest, Southeast, and East Coast are most at risk of exposure to extremely dangerous temperatures, meaning virtually the entire country is subject to increasing perils associated with heat exposure.

TERMINOLOGY

CDD - Cooling Degree Days
CMIP5 - Coupled Model Intercomparison Project version 5
CRN - Climate Reference Network
GCM - Global Climate Models
CONUS - Contiguous United States
EIA - Energy Information Administration (EIA)
GEE - Google Earth Engine
GSOM - Global Summaries of the Month
GHCND - Global Historical Climatology Network Daily
HI - Heat Index
INLA - Integrated Nested Laplace Approximation
kWh - Kilowatt Hours
LST - Land Surface Temperature
MACA - Multivariate Adaptive Constructed Analogs
MAE - Mean Absolute Error
NOAA - National Oceanic and Atmospheric Administration
NCEI - National Centers for Environmental Information
RCP - Representative Concentration Pathway
RECS - Residential Energy Consumption Survey
RH - Relative Humidity
RMSE - Root Mean Squared Error
SF - Scaling Factor
SPDE - Stochastic Partial Differential Equations
NWS - National Weather Service

METHODOLOGY

2.1 Data Sources

The First Street Extreme Heat Risk product is based on a number of data sources (Table 1). We relied to the fullest extent possible on open datasets from the U.S. Federal government to encourage reproducibility and further research efforts in the field. These sources are augmented with local and commercial sources when required to complete the heat risk product.

Table 1: Data Sources

Name	Subject	Source	Notes
Landsat 8	Land surface temperature	USGS	Open
USGS NED	Topography	USGS	Open
USGS NLCD	Land cover, impervious surface cover, canopy cover	USGS	Open
JRC Surface Water	Water bodies	Pekel et al., 2016	Open
MACAv2	Climate	Abatzoglou & Brown, 2012	Open, CMIP5 RCP4.5
Property Boundaries and characteristics	Descriptive information for properties	Lightbox	Aggregated from public records; Commercial but available
Building footprints	Building location on properties	Mapbox	Aggregated from satellite imagery and public records; Commercial but available
Energy Costs	State-level energy costs (kWh)	EIA	Open
Residential Energy Consumption Survey	Air conditioning electricity usage and cost information	EIA	Open

2.2 Local Heat Variability

The FSF-EHM model is dependent on a high resolution assessment of local heat variation. There is broad agreement in the scientific literature that air temperatures can exhibit distinct variation at scales of tens to hundreds of meters (Arnfield, 2003; Jenerette et al., 2011; Moffett et al., 2019; Stewart & Oke, 2012; W. Zhou et al., 2011). The urban heat island (UHI), or urban cool island (UCI) effects describe the elevation or diminution of temperatures relative to their surrounding area, driven by varying heat absorption and storage patterns among different land

surface types and urban layouts, as well as increased capture of anthropogenic heat sources (Kim & Brown, 2021; Stewart & Oke, 2012).

In general, meteorological station data does not provide a dense enough set of measurements to evaluate local air temperature variations with high fidelity. To address this limitation, our spatial model for mapping high resolution heat variation uses geospatial covariates to calibrate satellite derived land surface temperature (LST) estimates against in-situ temperature records from climate quality data stations. While LST is a distinct physical quantity from air temperature, the two values tend to be strongly correlated, and modeling approaches are well documented in existing heat research (Hoffman et al., 2020; Johnson et al., 2020; Moffett et al., 2019; Shandas et al., 2019; R. Shi et al., 2021; White et al., 2013; W. Zhou et al., 2011; Zhu et al., 2013). The full model is described in (Wilson et al., 2022) but key details are described below.

2.2.1 Data Processing

In the United States, the highest quality in situ temperature records are collected at 139 state-of-the-art CRN stations spread across CONUS, Hawaii, and Alaska (Rennie et al., 2021). Other high-quality national networks include the airport-based Automated Surface Observing System and Automated Weather Observing System, operated by the NWS and Federal Aviation Administration (Smith et al., 2011). Individual states, cities, or localities also operate additional “mesonet” networks that vary in size and area. The NOAA NCEI collates and applies expert quality control to many of these data streams into the GHCN and its associated information products (Menne et al., 2012).

To create a baseline air temperature dataset for our LST calibration, we acquired a consistent set of summertime monthly averaged daily maximum air temperature data from the NOAA GSOM version 1, a summary dataset derived from the NOAA Global Historical Climatology Network Daily dataset. All stations in the CONUS (n=7020) with complete June, July, and August monthly temperature records between 2014 and 2020 were used for model fitting to match the date range of Landsat 8, our source of LST data. For each station and month, we used the average temperature values across all 7 years of data as a single representative value for the complete time period.

We then acquired LST data from the Landsat 8 Collection 2 surface temperature product, which has an 8 day collection cycle and 30m spatial resolution. To construct a single composite image representing the average summertime land surface temperature across CONUS, we mosaic the median LST value for each 30m pixel across all Landsat 8 scenes with less than 15% cloud cover in June, July, and August between the years of 2014 and 2020 in Google Earth Engine. Taking the composite value across three months minimizes the probability of cloudy pixels affecting the median LST value. Each pixel has up to 80 potential cloud-free observations (92 days x 7 years / 8 day collection window) under this approach. Because each pixel’s median

value is dependent on the dates and temperature values of available images, more stringent thresholds (e.g. 5%) reduce sharp pixel-to-pixel artifacting that can occur when two neighboring pixels are drawing from images with different temperature values. However, stringent thresholds also create more areas with no-data values since fewer total images are considered in the mosaic. We chose a 15% cloud cover threshold after testing multiple different options from 5-25%, finding that it produced the smoothest mosaic with the fewest data quality issues. To fill in areas with missing data, we took an incremental approach where missing pixels were first filled with a 10 pixel spatial average, then a 4km spatial average, and finally a 50km spatial average.

The gridded covariates we used to calibrate the LST-surface air temperature relationship were chosen based on existing literature and include elevation, impervious surface cover, distance to water bodies, and distance to coastlines (Johnson et al., 2020; Kloog et al., 2014; L. Shi et al., 2016; D. Zhou et al., 2014; W. Zhou et al., 2011) (Table 2). Land-cover and tree-canopy cover were also considered as covariates during model testing, but were left out of the final model due to strong correlations with LST and impervious surface cover. The surface water layer was filtered to remove small ponds and streams that were unlikely to affect air temperature by imposing a neighborhood requirement of 10 interconnected 30m pixels, equivalent to a surface area of 9000 m^2. Surface water pixels that did not meet this threshold were converted to non-water pixels. We applied the same process to identify ocean pixels for the distance to the nearest coastline layer, using an extremely high threshold (50 million pixels) to exclude all water bodies except major oceans and their basins. Distance to coastlines and surface water were then calculated as the log transformed distance to the nearest water or coastline pixel.

Table 2: Model covariates

Variable:	**Source:**	**Resolution:**	**Units:**
Land Surface Temperature	Landsat 8	30m	Temperature (F)
Elevation	USGS National Elevation Database	10m	Meters
Impervious Surfaces	2016 USGS National Land Cover Database	30m	% Coverage in Pixel
Distance to Surface Water	Joint Research Center Global Surface Water	30m	Kilometers
Distance to Coastlines	Joint Research Center Global Surface Water	30m	Kilometers

To prepare covariate for model fitting, we extracted zonal statistics for all covariates in a 45m circular buffer around each climate data station, using the average value if multiple pixels were included in the buffer. These data were joined to the temperature records for each station.

2.2.2 Model Specification

The FSF-EHM uses a Stochastic Partial Differential Equations (SPDE) approach to modeling the spatial correlation between observed temperature records at climate data stations. Under this approach, air temperature is assumed to be a spatially continuous field that can be represented as a two-dimensional gaussian random field (GRF) with Matérn covariance, with station records defined as realizations of this field at known locations. The SPDE approach uses a high resolution triangulated grid to efficiently compute an approximation of GRF that can be defined for any points of interest (More information on the SPDE approach is provided in (Lindgren et al., 2011; Moraga et al., 2017).

Combining the covariate data described above with a triangulated mesh specified over CONUS, we define a spatial model for surface air temperature at station observations Y_i at locations x_i, *i=1,2 …, I with Equation (1):*

$$Y_i \sim Normal(\mu_i, \sigma^2),\ i = 1,\dots n,\ n+1,\ \dots\ n+m \qquad (1)$$
$$\mu_i = z_i\beta + S(x_i),\ i = 1,\dots,n$$

where $z_i = (1, z_i)$

is a vector of the intercept and covariates, β is a vector of coefficient values, and *S* is the value of the GRF at the station location modeled with a zero-mean Matern covariance function. The model is fit in R version 4.1 with the R package R-INLA, implementing the Integrated Nested Laplace Approximation (INLA), a computationally efficient alternative to Markov Chain Monte Carlo methods that performs approximate Bayesian inference (Rue et al., 2009). Coefficient values for all parameters are reported in Table 3.

We find that the 95% confidence intervals for all covariates are exclusive of zero, indicating consistent associations between most covariates and air temperature. Due to the different scales of covariates, the estimated coefficient values were not directly compared. However, our results show that temperatures are lower at higher elevations and near water bodies. Additionally, our estimates show a negative coefficient for impervious surface percentage, opposite of common directional associations for these variables seen in other heat research (Johnson et al., 2020; Moffett et al., 2019; W. Zhou et al., 2011) This effect reflects the interaction between LST, impervious surfaces, and air temperature in dense urban environments where LST can be greatly elevated compared to air temperatures. The estimates for the spatial random effect indicate large scale spatial dependence in the data, with fine scale spatial variance of approximately 17 km.

Table 3: Fitted model coefficients.

Parameter	***Mean***	***SD***
Intercept	41.01	9.4
LST (normalized)	36.15	1.4
Impervious Surfaces	-0.01	0.00
Elevation (km)	-0.01	0.00
Distance to Coastline (km), log-scale	1.23	.05
Distance to Surface Water (km), log-scale	0.01	.01
Range for Spatial Field	1985.15	415.16
Std. Dev for Spatial Field	17.2	0.72

To evaluate model performance, we implemented a k-fold (k=5) cross validation on out-of-sample in-situ station data (Figure 1). For this procedure, we split the station records into five folds of roughly equal size and iteratively fit the model to the remaining k-1 folds. For each iteration, we calculated the mean absolute error (MAE) and bias on the withheld observations, defined below.

$$\text{MAE} = \frac{1}{N}\sum_{i=1}^{N}\left|\left(Y_{i,\,predicted} - Y_{i,\,actual}\right)\right|$$

$$\text{BIAS} = \frac{1}{N}\sum_{i=1}^{N}\left(Y_{predicted} - Y_{actual}\right)$$

MAE is scale-dependent accuracy measures that reflects the magnitudes of out-of-sample prediction errors in the model. Bias is defined as the average difference between actual and predicted values and reflects whether predictions are systematically overestimated or underestimated. We averaged both metrics across all five iterations to provide robust measures of the out-of-sample prediction capability of the model, finding a MAE of 1.0 degrees F and a bias of 0.3 degrees F.

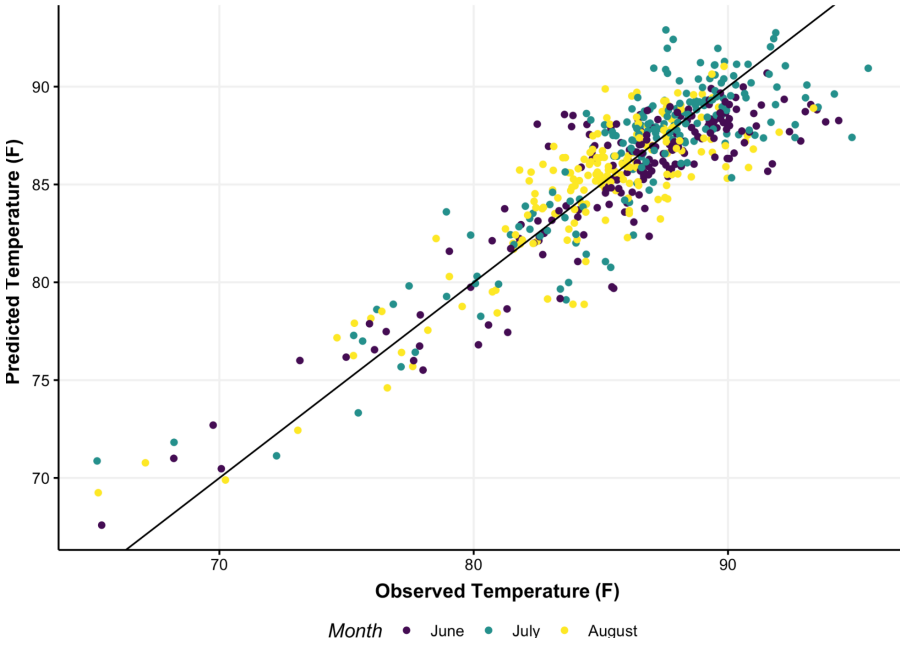

Figure 1: Cross validation results from [Wilson et al., 2022]

2.2.3 Comparison to field data

Wilson et al. 2022 also describes another validation procedure where we compared our 30m gridded predictions to an independent hyperlocal temperature map for the city of Durham from Climate Adaptation Planning Analytics (CAPA) Heat Watch (CAPA/NIHHIS, 2021). The CAPA Heat Watch product is a useful comparison because it uses different data sources from our model and the mapped area contains none of the in-situ climate data stations used for training our model.

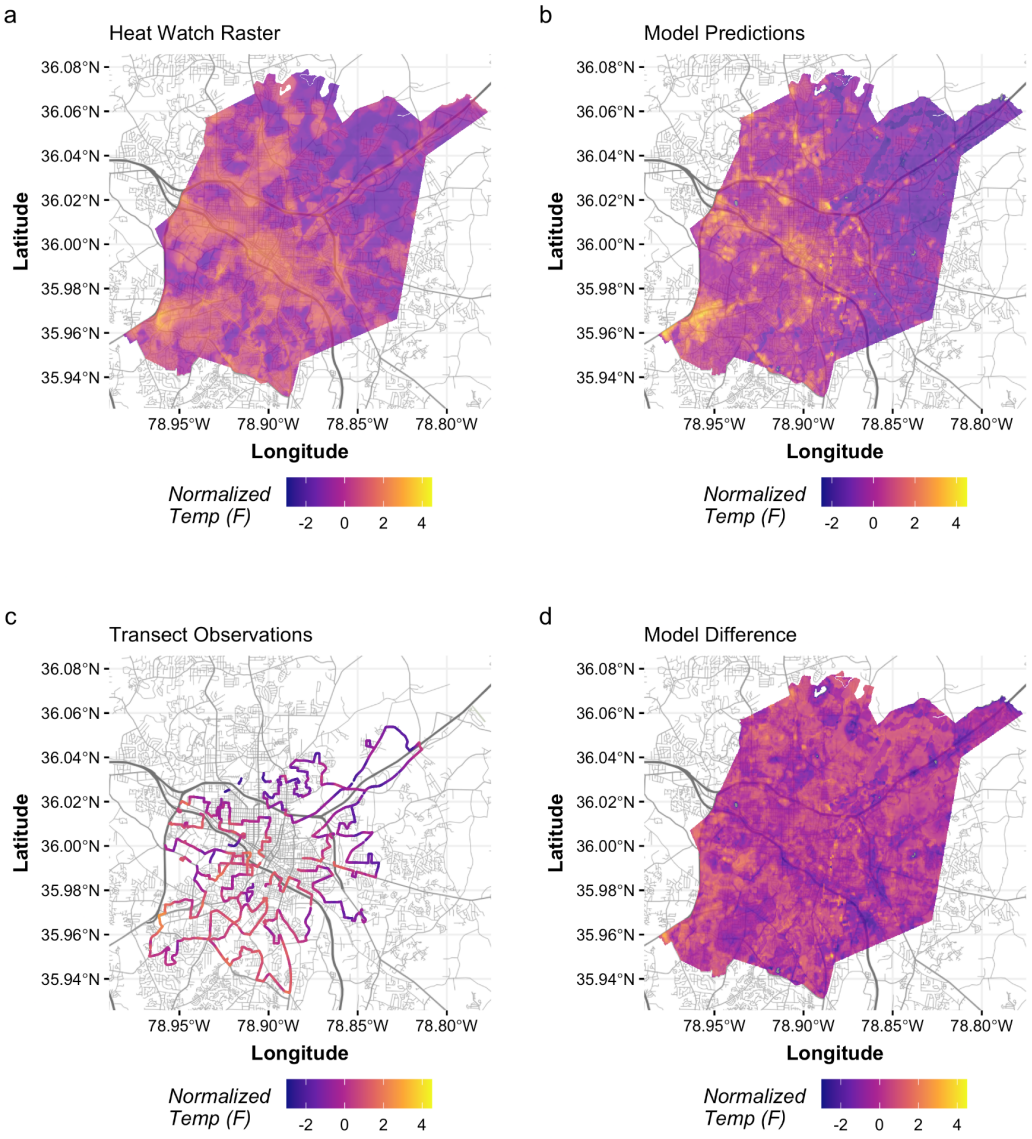

Figure 2: Normalized estimated temperatures from Heat Watch for July 23, 2021 (a) versus July model predictions (b) for Durham, North Carolina. Heat Watch transect routes are mapped in (c) and differences between models in (d). Figure from [(Wilson et al., 2022)]

For this analysis, we acquired the CAPA heat watch afternoon (3-4 pm) and evening temperature maps (7-8pm) and transect-based measurements for Durham (CAPA Heat Watch, 2021). These 10m gridded raster layers were produced by integrating thousands of in situ measurements collected by volunteers on July 23, 2021 with Sentinel II imagery . Full methodological details available in (Shandas et al., 2019). We selected the afternoon and evening time frames because they are more likely to correspond to the average daily maximum

temperature values outputted by our model compared to the morning collection window. We interpolated our 30m July predictions onto the 10m Heat Watch grid, standardizing both datasets to have zero mean and standard deviation of one to minimize the underlying differences in mean temperature resulting from the specific day of collection for the Heat Watch campaign. We then assessed the similarity between the two maps by computing the correlation coefficient on a pixel-by-pixel basis for both the afternoon and evening time window, finding a 0.50 and 0.75 correlation coefficients, respectively (Figure 2).

2.2.3 Climate scaling for 2053 conditions

Current twenty-first-century climate projections show increasing extreme heat exposure across CONUS (Broadbent et al., 2020; Meehl & Tebaldi, 2004; Rasmussen et al., 2016). To incorporate future climate conditions into our spatial model, we use a scaling factor approach in line with the First Street Foundation Flood and Wildfire models that statistically adjusts model output using an ensemble of downscaled CMIP5 GCMs. For the FSF-EHM we use an ensemble of 18 GCMS from the MACAv2 dataset (Abatzoglou & Brown, 2012) in scenario RCP4.5, excluding the two GCMs that are missing daily estimates of relative humidity. All GCMs and their original sources are listed in Table A1. We chose the RCP4.5 scenario to align with other First Street models and because it is a relatively middle-of-the-road carbon emissions scenario. Additionally, the spread in uncertainties among the ensemble results for different and more extreme CMIP5 RCPs (8.5, 2.6) generally overlap in the first 30 years of simulation.

For the FSF-EHM, scaling factors represent the projected percentage change in temperatures between current conditions (2017-2027) and future conditions (2047-2057). For each year-GCM combination, we convert a time series of daily maximum temperature values for current and future conditions to match the native output of our temperature model, the average maximum temperature in the hottest month of the year. This step ensures that the percentage change scaling factors are calibrated against the same time period as the underlying model output. For each pixel, we then average the mean maximum month temperatures across all year-GCM combinations and convert the output into a percentage difference between 2053 and 2023 conditions (Figure 3).

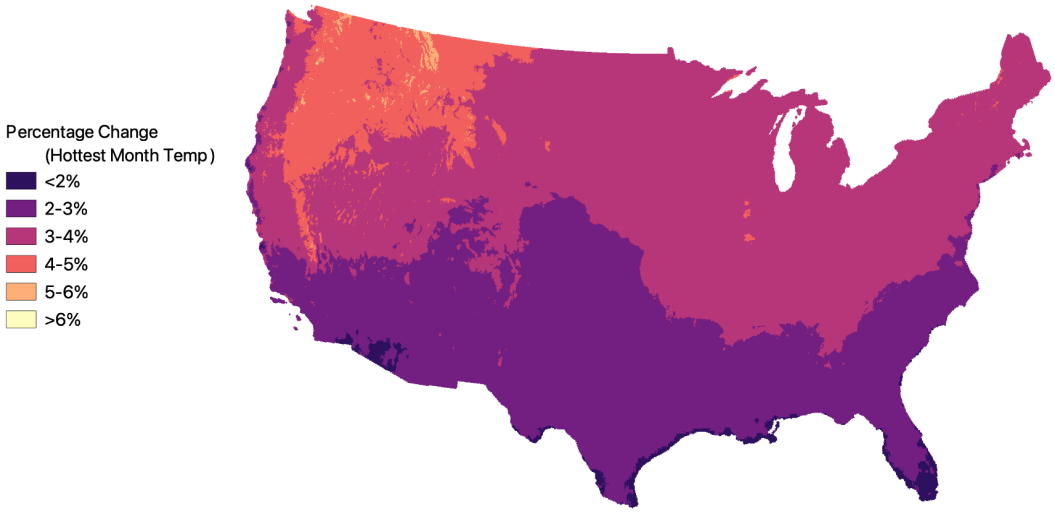

Figure 3: Scaling factor showing the percentage change in monthly averaged maximum temperatures under 2023 and 2053 conditions.

To generate 2053 predictions for our maximum month temperature model output, we multiply the scaling factors by our temperature predictions to return a scaled temperature value that estimates the projected increases in temperature in degrees Farenheit between 2023 and 2053 at 30m resolution. We add this temperature increase to the predictions for the current year to obtain 2053 estimates.

2.2.4 Conversion to temperature anomaly

The FSF-EHM natively outputs predictions at 30m resolution for the monthly averaged daily maximum temperature in July, the hottest month of the year across CONUS. We use this raster layer to derive a local temperature anomaly raster layer that reflects the temperature difference between each 30m pixel and a coarse regional temperature average at approximately 4 kilometer resolution. To create the coarse regional temperature layer, we apply a surface water mask to the July temperature layer and resample it onto the MACAv2 grid. We then interpolate this layer down to 500m resolution using a cubic spline interpolation and subtract it from the original 30m temperature raster. The resulting layer has units in degrees F and indicates whether each individual pixel pixel trends warmer or cooler compared to neighboring temperatures.

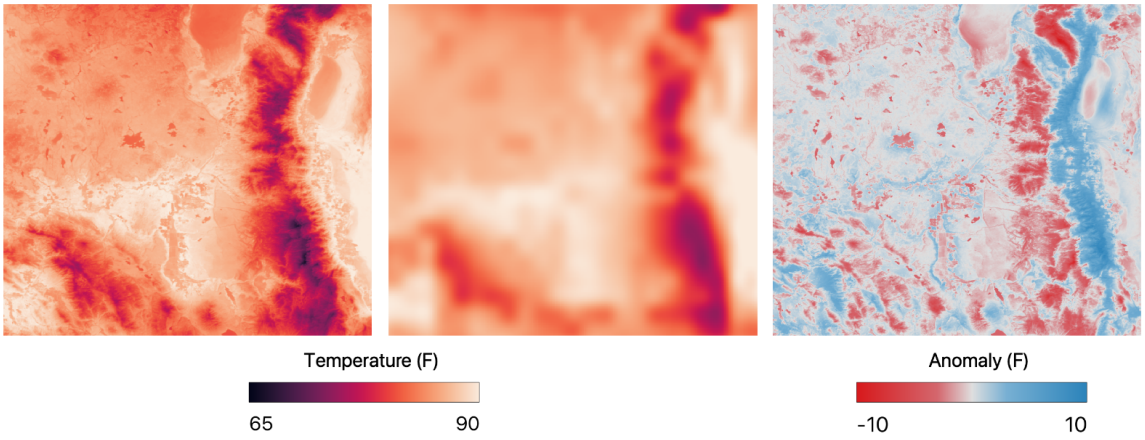

Figure 4: Example of anomaly creation. The high resolution (left) and lower resolution (center) are differenced to produce the anomaly (right).

2.3 Regional Heat Assessment

While air temperature shows variation at fine spatial scales, it is more common to assess temperature variation at coarser scales—typically at least several kilometers. Therefore, to supplement our high resolution temperature model we also derive a number of additional statistics at a lower resolution directly from the MACAv2 downscaled GCMs for both historical, current, and future conditions. Following recommendations in Abatzoglou and Brown (2012), we define the climatic baseline for temperature and relative humidity with MACAv2 historical projections from 1950-2005. This avoids inter-model variations in the baseline, since the MACAv2 downscaling process maps the statistics of the training data to the 1950-2005 period. For current and future conditions, we utilize the same ten year time series centered around 2023 (2017-2026) and 2053 (2047-2056) that we used for the scaling factor development. Using ten years of data for present and future conditions more accurately reflects long-term climate conditions and minimizes the variance associated with any single year. Unless otherwise specified, future usage of the terms ‘current’ and ‘future’ conditions refers to these ten-year time periods.

2.3.1 Defining local ‘hot days’

To establish a comparison baseline for each grid cell, we calculated the 98th percentile heat-index temperature value in each pixel for current conditions across all 18 downscaled GCMs using the in-built percentile reducer in Google Earth Engine. We selected the 98th percentile heat index temperature because it corresponds to the temperature value for which approximately seven days are in exceedance. This gives the 98th percentile temperature an intuitive explanation of the “hottest week” throughout the year, although there is no strict

requirement that the exceedance days occur consecutively. We term this heat index temperature value as the local 'hot day' for a given grid cell. We note that there may be some variations in these derived temperature values and observed temperature records due to our use of climate model projections from 2017-2027.

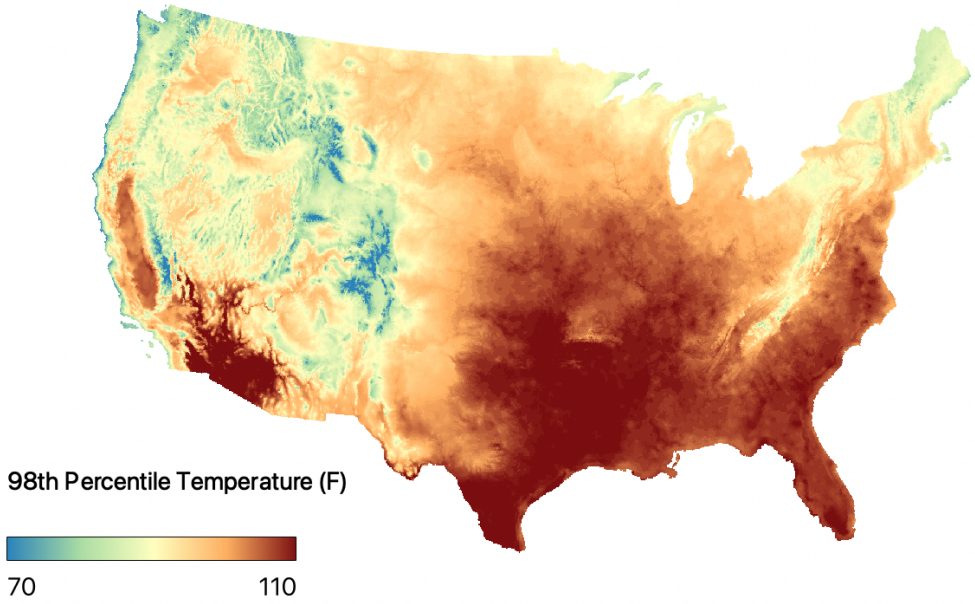

Figure 5: 98th percentile Heat Index temperature across CONUS

2.3.2 Heat Bins

To evaluate baseline changes in annual temperature distributions, we count the average number of days with max heat index values in the following bin ranges: <30, 30-40, 40-50, 50-60, 60-70, 70-80, 80-90, 90-100, 100-125, >125. We perform these calculations in GEE by converting the daily maximum temperature and minimum humidity values for each year-GCM combination into heat index temperatures, summing the total number of days in each bin range, and dividing by the number of year-GCM scenarios.

The top four bin ranges (80-90, 90-100, 100-125, and 125+) are set to closely mirror the National Weather Service's Heat Index warning classifications for caution, extreme caution, danger, and extreme danger (Figure 6 and Figure 7). In addition to counting days within each of these bin ranges individually, we sum the total number of days above 90 and 100 HI temperatures. We refer to days above 90/100 HI as health caution and dangerous days, respectively, informed by the NWS standards for vulnerable groups and the general population.

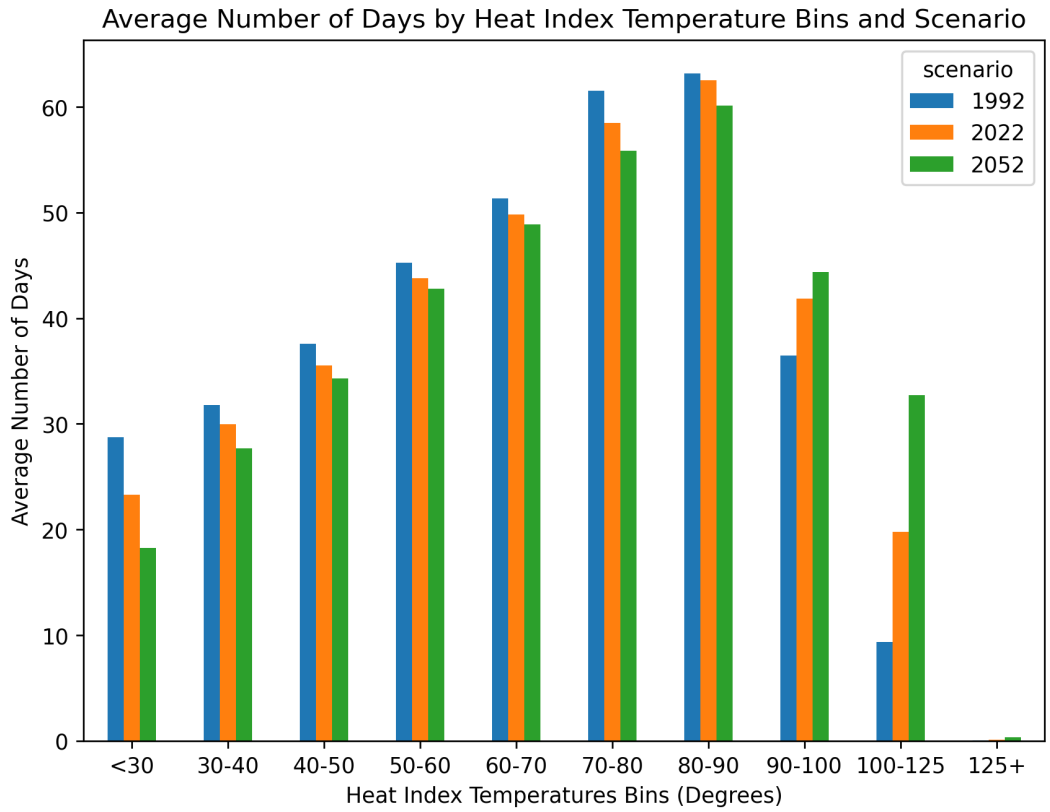

Figure 6: County-level averages of number of days by heat bin and time window.

The FSF-EHM finds that 99.97% of counties are likely to see at least one day of 80 degree heat index today and into the future with an average of around 135 days a year at this threshold, growing to 146 days in 30 years. Additionally, 98.86% of counties are likely to experience at least one day at a 90 degree heat index today with an average of 69 days at that temperature. That grows to an average of about 84 days in 30 years for about 99.54% of all counties in the US. Additionally, 91.03% of all counties are expected to experience at least one day above 100 degree heat index, growing to about 95.79% in 30 years. This change is also reflected in the average of 24 days of 100 degree temperature to grow to an average of 37 among all counties that are likely to experience this temperature. Finally, less than 1% of counties are likely to experience at least one day at 125 degree heat index today. However, that is likely to grow to about 26% of all counties experiencing at least one day in 30 years.

Table 4: Summary of heat threshold days

Metric	Definition	% Counties 2023*	% Counties 2053*	Average days 2023**	Average days 2053**
Caution Days	Heat index of 80°F or higher	99.97	99.97	135	146
Health Caution Days	Heat index of 90°F or higher	98.86	99.54	69	84
Dangerous Days	Heat index of 100 °F or higher	91.03	95.79	24	37
Extreme Danger Days	Heat index of 125°F or higher	0.29	26.07	1	1

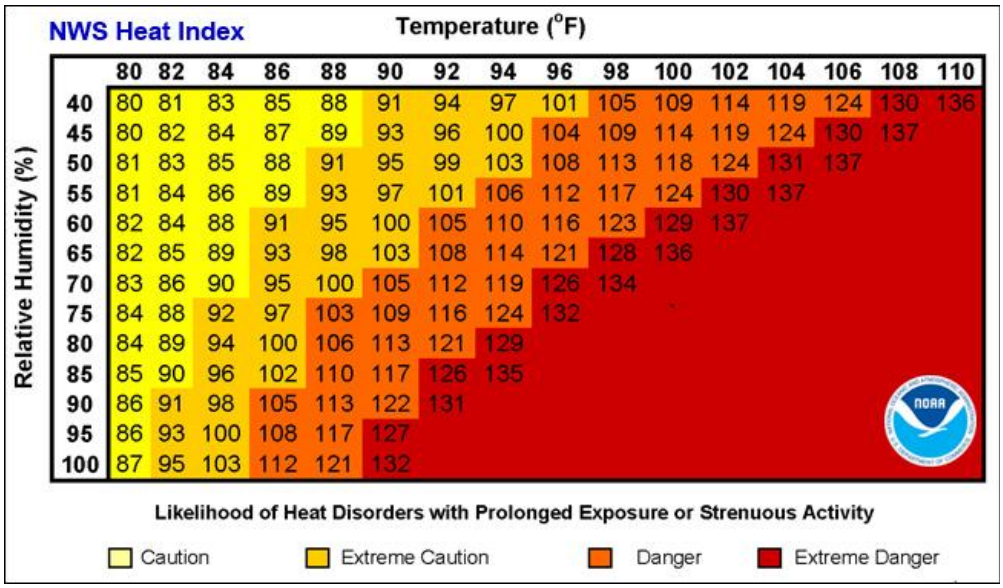

Figure 7: Heat safety categorizations per the NWS (https://www.weather.gov/ama/heatindex)

We also count the number of days above the 98th percentile heat index value for each pixel. For this statistic, we apply a downscaling procedure to localize the estimates onto our high resolution (30m) grid. We first calculate the 95th and 100th percentile temperatures for each pixel, as well as the temperature differences between the 95th and 98th percentile and the 98th and 100th percentile. We then implement the following procedure, leveraging the fact that a fixed number of days are spread between the 95th, 98th, and 100th percentile temperatures by definition:

1. Generate a sequence of values equal to the number of days above the 95th percentile using a cumulative sum distribution.
2. Scale this sequence by a breakpoint value that reflects the position of the 98th percentile temperature .
3. Subtract one from all values in the sequence so that the breakpoint value is zero.
4. Multiply the negative and positive values in the sequence by the temperature differences between the 95th-98th and 98th-100th percentiles, respectively.
5. Using the 30m anomaly layer, sum the number of values in the scaled sequences above or below the temperature anomaly (using positive sequence for a positive anomaly and vice versa).
6. Add or subtract the values from (5) to the number of days above the 98th percentile heat index value calculated at the coarse resolution.

To summarize, this procedure generates a series of temperature values for each day above the 95th percentile temperature that are scaled to the 95th-100th percentile temperature range and centered at the 98th percentile temperature. This sequence can be directly compared to the local temperature anomaly to count how many additional (or fewer) days at the 98th percentile would be expected with a given temperature anomaly. We use a cumulative sum distribution under the assumption that more days are allocated closer to the 95th percentile than the maximum temperature. For the current time period, there are 11 days between the 95th and 98th percentiles and 7 days between the 98th and 100th percentiles. For the future time period, we calculate the number of days above the current 98th percentile temperatures in GEE. For the days between the 95th and 98th percentile, we scale the days above 98th count by 1.57 to match the 11-7 ratio from the current period.

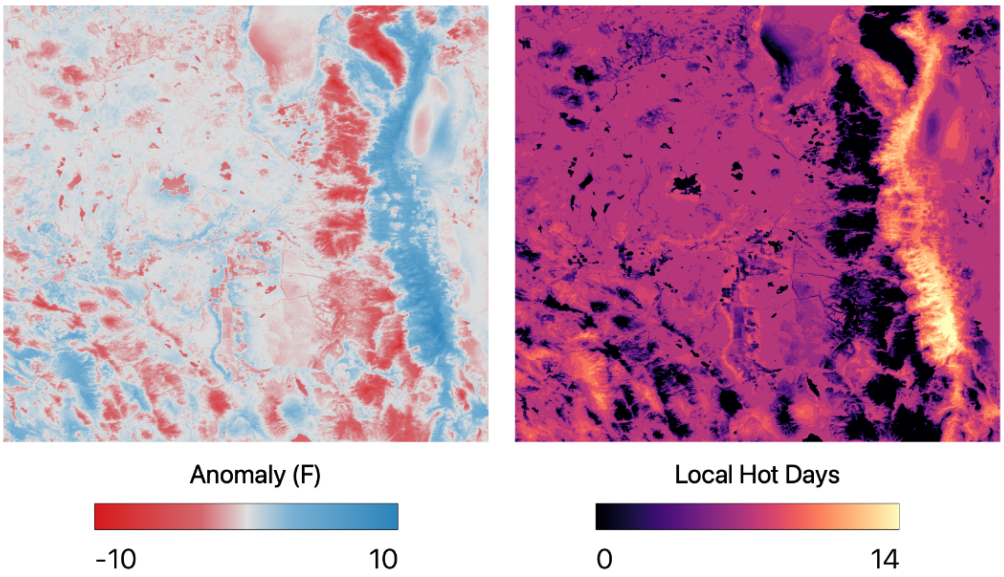

Figure 8: Example showing the temperature anomaly (left) and the downscaled local hot days (right).

2.3.3 Heat Waves

Heat waves, or consecutive periods of unusually hot weather, pose health risks for affected populations (Anderson & Bell, 2011; Raymond et al., 2020). To characterize heat wave exposures across CONUS, we define both absolute and relative thresholds. For absolute thresholds, we use five degree heat index increments from 90 to 110 degrees. For the relative threshold, we use the 98th percentile heat index temperature. For each threshold, we calculate two separate heat wave metrics: the longest continuous string of days with maximum temperature at or above the threshold with a 75% probability of occurrence, and the annual probability of any 3+ day period exceeding the threshold. All of the calculations are performed at the level of individual grid cells in the MACAv2 dataset, providing a horizontal resolution of approximately 4km.

To calculate the maximum continuous string of days for each pixel, we use the same daily Heat Index time series used for the binned days computations. Within each year-GCM time series, we identify the day of year values above each heat wave threshold and use a forward differencing algorithm in GEE to extract the length of the longest continuous run. Repeating this procedure for all year-GCMs combinations generates an empirical distribution of the maximum string of consecutive days above each threshold for each pixel. From these distributions, we take the value at the 25th empirical quartile to represent the expected duration of consecutive days occurring with 75% probability, and take the sum of scenarios with a 3+ day heat wave

divided by the total scenarios as the annual probability of any heat wave. This entire procedure is performed on the historical, current, and future MACAv2 time series.

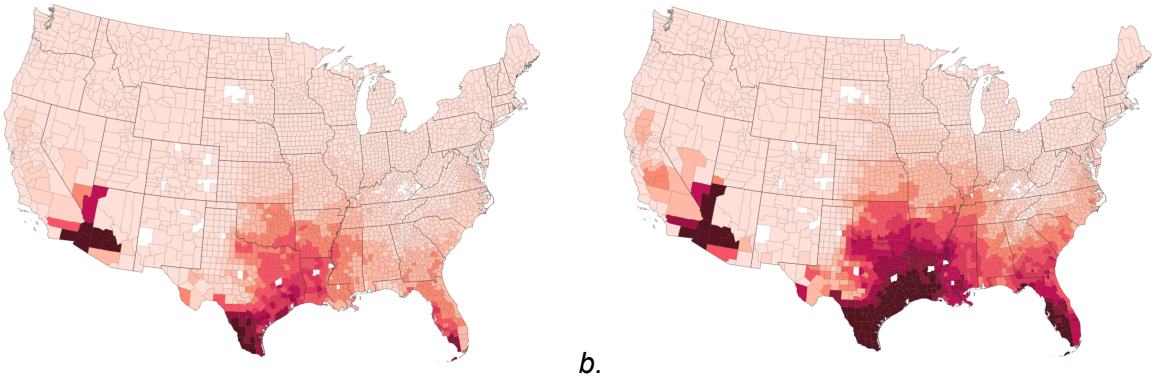

a. *b.*

Figure 9. Length of Consecutive Dangerous Days (above 100°F) 2023(a), 2053(b)

2.4 Risk Score Assignment

The Heat Factor risk assessment was completed on a property-level basis across CONUS using property parcel geometries from Lightbox public-record property boundaries. To calculate a 30-year, climate adjusted heat risk score for each property, we first account for humidity differences across CONUS by converting our average maximum month temperature data into Heat Index values using the average minimum humidity values in July for 2023 and 2053 from the MACAv2 downscaled GCMs. We then average the heat index temperatures across the current and future scenarios, assuming a linear interpolation across the 30 year time period. The Heat Factor score is assigned to each parcel centroid based on the heat index temperature breakpoints in Table 5, which are equally spaced across 3 degree bins, increasing to 6 degree bins for the upper score ranges to capture the right tail of the distribution. The distribution of Heat Factor scores is shown in Figure 10.

Table 5: Heat Factor score breakpoints

Mean Heat Index in July	Heat Factor Score
Less than 80	1
80 - 83	2
83 - 86	3
86 - 89	4
89 - 92	5
92 - 95	6
95 - 98	7
98 - 104	8
104 - 110	9
Greater than 110	10

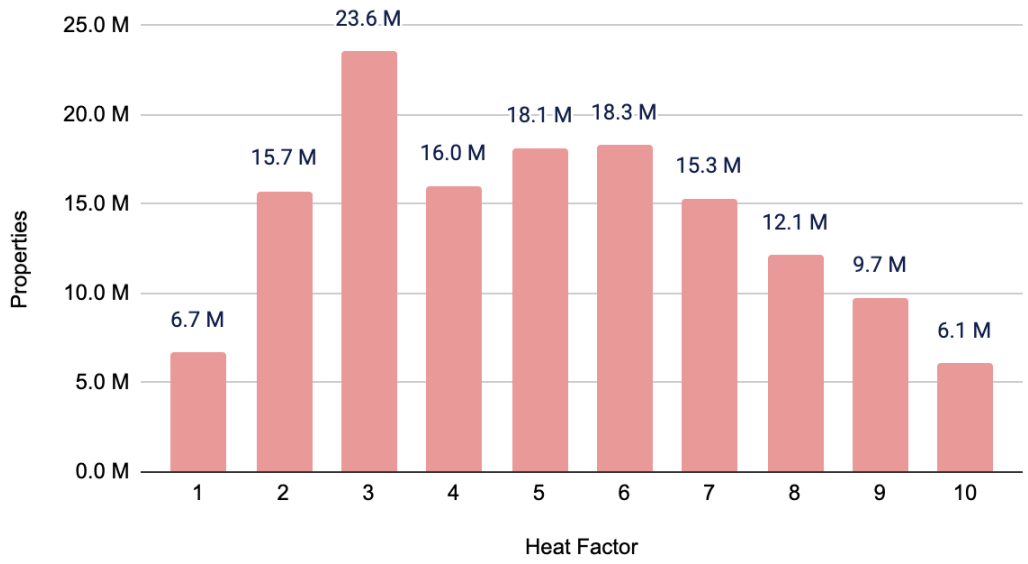

Figure 10: Distribution of Risk Factor Scores

2.5 Property-Level Energy Usage for Air Conditioning

To further communicate the impacts of rising temperatures across the United States, we quantify how air conditioning (AC) costs on electricity bills at individual properties may be affected under a changing climate. As temperatures increase into summer months each year, most properties spend more on electricity due to an increased use in air conditioning. We model the electricity consumption for both residential and commercial properties in current and future conditions to show how the AC costs will change for any property over the next three decades. We note that our calculations only consider air conditioning costs and do not account for reductions in heating costs or other electricity usage. Research shows mixed results on whether the United States will see net increases or reductions in total energy costs under climate change (Hsiang et al., 2017; Reidmiller et al., 2018; Rode et al., 2021).

2.5.1 Residential Modeling

The Energy Information Administration (EIA) distributes energy information and data to aid policymakers, markets, and to the public to aid in the understanding of energy. We use microdata from the 2015 EIA Residential Energy Consumption Survey (RECS) to construct our energy consumption and cost models. The 2015 survey vintage uses data collected in 2015 and 2016 and is the most recently available source of energy consumption data. The next survey collection period started in 2020 and is expected to be finalized by 2023. The 2015 RECS survey contains property level information on energy consumption, energy prices, and property characteristics (such as age of home, square footage, number of bedrooms, etc.). The surveyed properties were randomly selected through a multistage, area-probability sample design (n=5,686) . The final sample represents 118.2 million U.S. residential households and only sampling homes that are used as a primary residence. Vacation homes, vacant units, or common areas in residential buildings are not included. This makes the RECS survey an ideal indicator for making comparisons of different characteristics of homes and their energy usage across the residential sector.

Due to the nature of this survey, within each variable there are imputed responses where data were missing. Imputations were calculated by the EIA when responses were “Dont Know” or “Refuse”. We refer readers to the EIA website in order to review imputation methodology on the microdata. The EIA recommends that imputed data should be used to avoid biased estimations. Therefore, no data points were dropped which had imputation flags. Imputation rates in the survey are low, with the average rate being around 3.7%. 81% of variables had an imputation rate less than 5%, and 94% had imputation rates less than 10%. We exclude responses with zero consumption, leaving 4,948 residential properties available as inputs to the model.

We constructed a multivariate linear regression model to estimate AC electricity consumption in homes around the nation. We included covariates on square footage, year built, latitude (taken as the average latitude within a climate zone), and cooling degree days (CDD). CDD is defined as the annual sum of the daily temperature differential between the average daily temperature and 65 degrees. Square footage and year built are included as property-specific predictors that reflect expected AC usage and efficiency. Latitude and CDD provide information on the location of the home and annual temperature ranges. Both square footage and CDD are log transformed in our regression to handle skewness. We recode the categorical year-built variable from 1-8 to reflect the corresponding decades, where 1=1940, … , 8=2010. For privacy reasons, property-specific information is stripped from the microdata, so we assign each property the average latitude of the IECC climate zone that it resides in.

Table 6. Residential regression results

Goodness of Fit Metrics	
R-Squared	0.704
Mean Absolute Error (MAE)	816 kWH annually
MAE Converted to Dollars	Approximately $90 annually

	Coefficient	p-Value
Intercept	11.057852	7.234393e-38
log(square footage)	0.861165	0
log(cooling degree days)	0.949135	0
year built	-0.007721	7.315957e-75
latitude	-0.054003	1.268557e-63

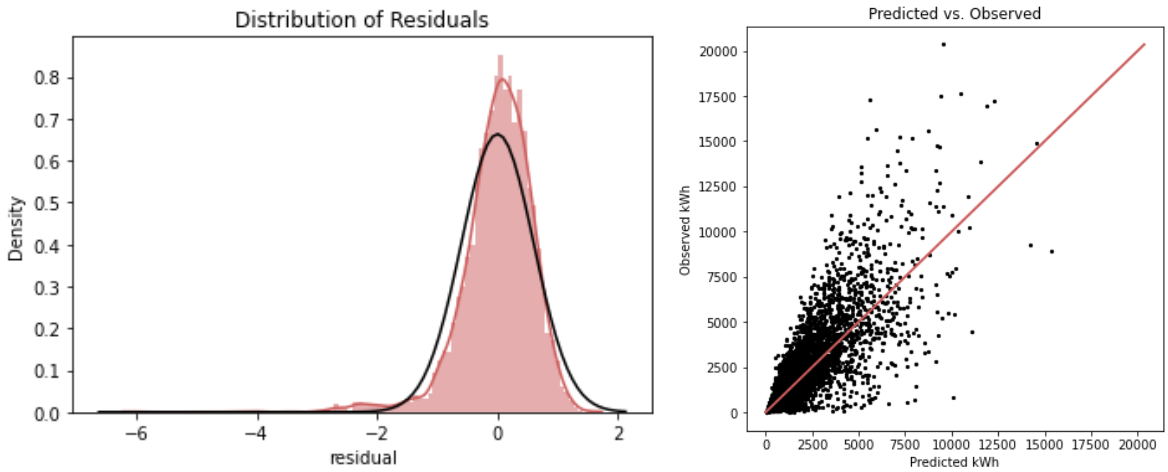

Figure 11: Distribution of Residuals and Predicted vs. Observed From Residential Regression

2.5.2 Commercial Modeling

We adopted the same modeling approach for commercial buildings, using the 2012 EIA commercial survey microdata. Per the EIA website, consumption and expenditures will be available in the spring of 2022, but were not available at the time of publication. Subsequent updates to the FSF-EHM may include new survey data as it becomes available. The 2012 survey contains 6,720 records of commercial properties along with their building characteristics and electricity consumption used for air conditioning. All 50 states are represented and the sample of 6,720 records is estimated to represent 5.6 million commercial buildings in the United States. We dropped any properties with zero consumption, leaving 5844 records for commercial properties.

Similarly to the residential survey, the smallest geographic detail available is census division and there are no state level identifiers to protect the privacy and confidentiality of individual buildings. We also used a multivariate linear regression to estimate electricity consumption among commercial buildings around the United States. The methodology is the same as the residential regression, except for a few covariate updates. The commercial regression removed latitude and year built as covariates and added the type of business as a factor. We still took the log of the square footage, cooling degree days, and consumption.

Table 7: Commercial regression results

Goodness of Fit Metrics	
R-Squared	0.819
Mean Absolute Error (MAE)	369,236 kWH annually
MAE Converted to Dollars	Approximately $40,000 annually

	Coefficient	p-Value
Intercept	-8.953038	0.000000e+00
log(square footage)	1.063462	0.000000e+00
log(cooling degree days)	0.925487	0.000000e+00
C(building_activity)[T.2]: Office	1.983734	1.846983e-57
C(building_activity)[T.4]: Laboratory	3.596831	3.457459e-63
C(building_activity)[T.5]: Nonrefrigerated Warehouse	0.360003	4.822029e-03
C(building_activity)[T.6]: Food Sales	1.966550	3.108001e-37
C(building_activity)[T.7]: Public Order/Safety	1.964525	1.551228e-33
C(building_activity)[T.8]: Outpatient Health Care16	1.648258	6.528716e-31
C(building_activity)[T.11]: Refrigerated Warehouse	0.237801	4.088881e-01
C(building_activity)[T.12]: Religious Worship	1.154493	4.819072e-18
C(building_activity)[T.13]: Public Assembly	2.617631	1.276368e-84
C(building_activity)[T.14]: Education	1.980533	2.030842e-54
C(building_activity)[T.15]: Food Service	2.873862	2.478810e-99
C(building_activity)[T.16]: Inpatient Health Care	3.048313	1.246303e-110
C(building_activity)[T.17]: Nursing	2.451635	8.313179e-51
C(building_activity)[T.18]: Lodging	1.486850	8.839176e-28
C(building_activity)[T.23]: Strip Shopping Mall	2.145675	1.718559e-56
C(building_activity)[T.24]: Enclosed Mall	1.953123	3.814574e-19
C(building_activity)[T.25]: Retail Other Than Mall	1.721725	3.134479e-38
C(building_activity)[T.26]: Service	1.339534	1.779810e-23

C(building_activity)[T.91]: Other	1.405296	6.961076e-16

2.5.3 Cost Conversions

We calculated the air conditioning costs in kWh for every property across CONUS using the coefficients from our multiple regressions described above. We used building characteristic data from Lightbox (year built, square footage, land use codes) for the predictions, with land use codes mapped to the EIA land use information for commercial predictions. Latitude was taken at the centroid of the parcel for each property. Cooling degree days were derived for every property using our heat bin data with a baseline cooling temperature of 70 degrees.

In order to translate our consumption predictions in kWh into AC costs, we used historical data on average electricity costs at the state level from the EIA. This data provides provides the average cost of electricity in cents per kWh for each state from 1990 to present by residential or commercial property types and can be found in the EIA Monthly Form EIA-861M: https://www.eia.gov/electricity/data.php#summary. Residential and commercial electricity costs are considered separately using the corresponding EIA price information. To calculate a base level energy cost for air conditioning specifically, we took the average over the past five years (2016-2021) for each state and only used the months of June-September, or the months when air conditioning usage would be typical in the U.S. Residential and commercial costs for each state are shown in Table 8.

Table 8: Residential and commercial energy costs by state (cents/kWh)

State Code	Residential Price	Commercial Price
AK	22.953	19.421
AL	12.809	11.663
AR	10.617	8.667
AZ	12.654	10.903
CA	20.486	19.056
CO	12.809	10.911
CT	21.591	16.487
DC	12.525	11.964
DE	12.483	9.262
FL	11.659	9.132
GA	12.763	10.267
HI	31.234	28.669
IA	13.865	11.133

ID	10.400	8.108
IL	12.695	9.205
IN	12.763	10.990
KS	13.235	10.728
KY	10.967	10.147
LA	10.190	9.0695
MA	21.315	16.789
MD	13.145	9.9475
ME	17.006	12.375
MI	16.371	11.531
MN	13.898	11.277
MO	12.806	10.411
MS	11.130	10.239
MT	11.605	10.471
NC	11.402	8.739
ND	12.071	9.675
NE	11.807	9.354
NH	19.3675	15.461
NJ	15.982	12.904
NM	13.502	10.844
NV	11.469	7.969
NY	19.048	16.209
OH	12.695	9.795
OK	10.765	8.525
OR	11.268	8.862
PA	13.940	8.706
RI	19.882	15.438
SC	12.905	10.456
SD	12.635	10.048
TN	10.877	10.718
TX	11.527	8.010
UT	10.925	8.748
VA	12.305	8.012
VT	18.365	15.747
WA	10.043	8.777
WI	14.467	11.021

WV	11.804	9.153
WY	11.936	9.841

Appendix:

Heat Index Conversion:

Humidity plays an important role in how heat is 'experienced' at local scales. To account for humidity in our supplemental statistics, we convert daily temperature and humidity measures from each GCMs into Heat Index values (apparent temperature in degrees F) using the modified Rothfusz regression equations (https://www.wpc.ncep.noaa.gov/html/heatindex_equation.shtml).

The base equation is defined as follows:

(1): HI = - 42.379 + 2.04901523 * T + 10.14333127 * RH - 0.22475541 * T * RH - .00683783 * T * T - .05481717 * RH * RH + .00122874 * T * T * RH + 0.00085282 * T * RH * RH - .00000199 * T * T * RH * RH

where T is temperature in degrees F and RH is relative humidity in percent. If the RH is less than 13% and the temperature is between 80 and 112 degrees F, then the following adjustment is subtracted from HI:

(2): ADJUSTMENT = [(13 - *RH*) / 4] * SQRT{[17 - ABS(T - 95.)] / 17}

If the RH is greater than 85% and the temperature is between 80 and 87 degrees F, then the following adjustment is added to HI:

(3): ADJUSTMENT = [(RH - 85) / 10] * [(87 - T) / 5]

For Heat Index Values below 80 degrees F, an alternate formula is applied to calculate values consistent with Steadman's results:

(4) HI = 0.5 * {T + 61.0 + [(T - 68.0) * 1.2] + (RH * 0.094)}

Global Climate Model Details:

Information on the global climate models downscaled via the MACA approach are provided in Table A1. We excluded the two models that do not have daily estimates of relative humidity (CCSM4 and NorESM1-M).

Table A1: Information on the climate model used for the FSF-EHM
(https://climate.northwestknowledge.net/MACA/GCMs.php)

The 20 models used for MACA downscaling are:

Model Name	Model Country	Model Agency	Atmosphere Resolution(Lon x Lat)	Ensemble Used
bcc-csm1-1	China	Beijing Climate Center, China Meteorological Administration	2.8 deg x 2.8 deg	r1i1p1
bcc-csm1-1-m	China	Beijing Climate Center, China Meteorological Administration	1.12 deg x 1.12 deg	r1i1p1
BNU-ESM	China	College of Global Change and Earth System Science, Beijing Normal University, China	2.8 deg x 2.8 deg	r1i1p1
CanESM2	Canada	Canadian Centre for Climate Modeling and Analysis	2.8 deg x 2.8 deg	r1i1p1
CCSM4	USA	National Center of Atmospheric Research, USA	1.25 deg x 0.94 deg	r6i1p1
CNRM-CM5	France	National Centre of Meteorological Research, France	1.4 deg x 1.4 deg	r1i1p1
CSIRO-Mk3-6-0	Australia	Commonwealth Scientific and Industrial Research Organization/Queensland Climate Change Centre of Excellence, Australia	1.8 deg x 1.8 deg	r1i1p1
GFDL-ESM2M	USA	NOAA Geophysical Fluid Dynamics Laboratory, USA	2.5 deg x 2.0 deg	r1i1p1
GFDL-ESM2G	USA	NOAA Geophysical Fluid Dynamics Laboratory, USA	2.5 deg x 2.0 deg	r1i1p1
HadGEM2-ES	United Kingdom	Met Office Hadley Center, UK	1.88 deg x 1.25 deg	r1i1p1
HadGEM2-CC	United Kingdom	Met Office Hadley Center, UK	1.88 deg x 1.25 deg	r1i1p1
inmcm4	Russia	Institute for Numerical Mathematics, Russia	2.0 deg x 1.5 deg	r1i1p1
IPSL-CM5A-LR	France	Institut Pierre Simon Laplace, France	3.75 deg x 1.8 deg	r1i1p1
IPSL-CM5A-MR	France	Institut Pierre Simon Laplace, France	2.5 deg x 1.25 deg	r1i1p1
IPSL-CM5B-LR	France	Institut Pierre Simon Laplace, France	2.75 deg x 1.8 deg	r1i1p1
MIROC5	Japan	Atmosphere and Ocean Research Institute (The University of Tokyo), National Institute for Environmental Studies,and Japan Agency for Marine-Earth Science and Technology	1.4 deg x 1.4 deg	r1i1p1
MIROC-ESM	Japan	Japan Agency for Marine-Earth Science and Technology, Atmosphere and Ocean Research Institute (The University of Tokyo), and National Institute for Environmental Studies	2.8 deg x 2.8 deg	r1i1p1
MIROC-ESM-CHEM	Japan	Japan Agency for Marine-Earth Science and Technology, Atmosphere and Ocean Research Institute (The University of Tokyo), and National Institute for Environmental Studies	2.8 deg x 2.8 deg	r1i1p1
MRI-CGCM3	Japan	Meteorological Research Institute, Japan	1.1 deg x 1.1 deg	r1i1p1
NorESM1-M	Norway	Norwegian Climate Center, Norway	2.5 deg x 1.9 deg	r1i1p1

References:

Abatzoglou, J. T., & Brown, T. J. (2012). A comparison of statistical downscaling methods suited for wildfire applications: STATISTICAL DOWNSCALING FOR WILDFIRE APPLICATIONS. *International Journal of Climatology*, *32*(5), 772–780. https://doi.org/10.1002/joc.2312

Anderson, G. B., & Bell, M. L. (2011). Heat Waves in the United States: Mortality Risk during Heat Waves and Effect Modification by Heat Wave Characteristics in 43 U.S. Communities. *Environmental Health Perspectives*, *119*(2), 210–218. https://doi.org/10.1289/ehp.1002313

Armal, S., Porter, J. R., Lingle, B., Chu, Z., Marston, M. L., & Wing, O. E. (2020). Assessing property level economic impacts of climate in the US, new insights and evidence from a comprehensive flood risk assessment tool. Climate, 8(10), 116.

Arnfield, A. J. (2003). Two decades of urban climate research: A review of turbulence, exchanges of energy and water, and the urban heat island. *International Journal of Climatology*, *23*(1), 1–26. https://doi.org/10.1002/joc.859

Bates, P. D., Quinn, N., Sampson, C., Smith, A., Wing, O., Sosa, J., ... & Krajewski, W. F. (2021). Combined modeling of US fluvial, pluvial, and coastal flood hazard under current and future climates. Water Resources Research, 57(2), e2020WR028673.

Broadbent, A. M., Krayenhoff, E. S., & Georgescu, M. (2020). The motley drivers of heat and cold exposure in 21st century US cities. *Proceedings of the National Academy of Sciences*, *117*(35), 21108–21117. https://doi.org/10.1073/pnas.2005492117

CAPA/NIHHIS. (2021). *Heat Watch Raleigh—Durham (2021)*. https://osf.io/rwjnx/

Garrick, B. J., & Kaplan, S. (1981). On the quantitative definition of risk. *Risk Analysis*, *1*(1), 11-27.

Hoffman, J. S., Shandas, V., & Pendleton, N. (2020). The Effects of Historical Housing Policies on Resident Exposure to Intra-Urban Heat: A Study of 108 US Urban Areas. *Climate*, *8*(12). https://doi.org/10.3390/cli8010012

Hsiang, S., Kopp, R., Jina, A., Rising, J., Delgado, M., Mohan, S., Rasmussen, D. J., Muir-Wood, R., Wilson, P., Oppenheimer, M., Larsen, K., & Houser, T. (2017). Estimating economic damage from climate change in the United States. *Science*, *356*(6345), 1362–1369. https://doi.org/10.1126/science.aal4369

Jenerette, G. D., Harlan, S. L., Stefanov, W. L., & Martin, C. A. (2011). Ecosystem services and urban heat riskscape moderation: Water, green spaces, and social inequality in Phoenix, USA. *Ecological Applications: A Publication of the Ecological Society of America*, *21*(7), 2637–2651. https://doi.org/10.1890/10-1493.1

Johnson, S., Ross, Z., Kheirbek, I., & Ito, K. (2020). Characterization of intra-urban spatial variation in observed summer ambient temperature from the New York City Community Air Survey. *Urban Climate*, *31*, 100583. https://doi.org/10.1016/j.uclim.2020.100583

Kearns, E. J., Amodeo, M., Chadwick, S., Eby, M., & Porter, J. R. (2020, December). Making Climate Change Personal: Enabling Action Through Communication of Flood Risk Science to Individuals. In AGU Fall Meeting Abstracts (Vol. 2020, pp. SY040-06).

Kim, S. W., & Brown, R. D. (2021). Urban heat island (UHI) intensity and magnitude estimations: A systematic literature review. *Science of The Total Environment*, *779*, 146389. https://doi.org/10.1016/j.scitotenv.2021.146389

Kloog, I., Nordio, F., Coull, B. A., & Schwartz, J. (2014). Predicting spatiotemporal mean air

temperature using MODIS satellite surface temperature measurements across the Northeastern USA. *Remote Sensing of Environment*, *150*, 132–139. https://doi.org/10.1016/j.rse.2014.04.024

Lindgren, F., Rue, H., & Lindström, J. (2011). An explicit link between Gaussian fields and Gaussian Markov random fields: The stochastic partial differential equation approach. *Journal of the Royal Statistical Society: Series B (Statistical Methodology)*, *73*(4), 423–498. https://doi.org/10.1111/j.1467-9868.2011.00777.x

Meehl, G. A., & Tebaldi, C. (2004). More Intense, More Frequent, and Longer Lasting Heat Waves in the 21st Century. *Science*, *305*(5686), 994–997. https://doi.org/10.1126/science.1098704

Menne, M. J., Durre, I., Vose, R. S., Gleason, B. E., & Houston, T. G. (2012). An Overview of the Global Historical Climatology Network-Daily Database. *Journal of Atmospheric and Oceanic Technology*, *29*(7), 897–910. https://doi.org/10.1175/JTECH-D-11-00103.1

Moffett, K. B., Makido, Y., & Shandas, V. (2019). Urban-Rural Surface Temperature Deviation and Intra-Urban Variations Contained by an Urban Growth Boundary. *Remote Sensing*, *11*(22), 2683. https://doi.org/10.3390/rs11222683

Moraga, P., Cramb, S. M., Mengersen, K. L., & Pagano, M. (2017). A geostatistical model for combined analysis of point-level and area-level data using INLA and SPDE. *Spatial Statistics*, *21*, 27–41. https://doi.org/10.1016/j.spasta.2017.04.006

Pekel, JF., Cottam, A., Gorelick, N. *et al.* (2016). High-resolution mapping of global surface water and its long-term changes. *Nature* 540, 418−422.

Rasmussen, D. J., Meinshausen, M., & Kopp, R. E. (2016). Probability-Weighted Ensembles of U.S. County-Level Climate Projections for Climate Risk Analysis. *Journal of Applied Meteorology and Climatology*, *55*(10), 2301–2322. https://doi.org/10.1175/JAMC-D-15-0302.1

Raymond, C., Matthews, T., & Horton, R. M. (2020). The emergence of heat and humidity too severe for human tolerance. *Science Advances*, *6*(19), eaaw1838. https://doi.org/10.1126/sciadv.aaw1838

Reidmiller, D. R., Avery, C. W., Easterling, D. R., Kunkel, K. E., Lewis, K. L. M., Maycock, T. K., & Stewart, B. C. (2018). *Impacts, Risks, and Adaptation in the United States: The Fourth National Climate Assessment, Volume II*. U.S. Global Change Research Program. https://doi.org/10.7930/NCA4.2018

Rennie, J. J., Palecki, M. A., Heuser, S. P., & Diamond, H. J. (2021). Developing and Validating Heat Exposure Products Using the U.S. Climate Reference Network. *Journal of Applied Meteorology and Climatology*, *60*(4), 543–558. https://doi.org/10.1175/JAMC-D-20-0282.1

Rode, A., Carleton, T., Delgado, M., Greenstone, M., Houser, T., Hsiang, S., Hultgren, A., Jina, A., Kopp, R. E., McCusker, K. E., Nath, I., Rising, J., & Yuan, J. (2021). Estimating a social cost of carbon for global energy consumption. *Nature*, *598*(7880), 308–314. https://doi.org/10.1038/s41586-021-03883-8

Rue, H., Martino, S., & Chopin, N. (2009). Approximate Bayesian inference for latent Gaussian models by using integrated nested Laplace approximations. *Journal of the Royal Statistical Society: Series B (Statistical Methodology)*, *71*(2), 319–392. https://doi.org/10.1111/j.1467-9868.2008.00700.x

Shandas, V., Voelkel, J., Williams, J., & Hoffman, J. (2019). Integrating Satellite and Ground Measurements for Predicting Locations of Extreme Urban Heat. *Climate*, *7*(1), 5. https://doi.org/10.3390/cli7010005

Shi, L., Liu, P., Kloog, I., Lee, M., Kosheleva, A., & Schwartz, J. (2016). Estimating daily air temperature across the Southeastern United States using high-resolution satellite data: A statistical modeling study. *Environmental Research*, *146*, 51–58.

https://doi.org/10.1016/j.envres.2015.12.006
Shi, R., Hobbs, B. F., Zaitchik, B. F., Waugh, D. W., Scott, A. A., & Zhang, Y. (2021). Monitoring intra-urban temperature with dense sensor networks: Fixed or mobile? An empirical study in Baltimore, MD. *Urban Climate*, *39*, 100979. https://doi.org/10.1016/j.uclim.2021.100979
Smith, A., Lott, N., & Vose, R. (2011). The Integrated Surface Database: Recent Developments and Partnerships. *Bulletin of the American Meteorological Society*, *92*(6), 704–708.
Stewart, I. D., & Oke, T. R. (2012). Local Climate Zones for Urban Temperature Studies. *Bulletin of the American Meteorological Society*, *93*(12), 1879–1900. https://doi.org/10.1175/BAMS-D-11-00019.1
White, -Newsome Jalonne L., Brines, S. J., Brown, D. G., Dvonch, J. T., Gronlund, C. J., Zhang, K., Oswald, E. M., & O, 'Neill Marie S. (2013). Validating Satellite-Derived Land Surface Temperature with in Situ Measurements: A Public Health Perspective. *Environmental Health Perspectives*, *121*(8), 925–931. https://doi.org/10.1289/ehp.1206176
Wilson, B., Porter, J. R., Kearns, E. J., Hoffman, J. S., Shu, E., Lai, K., Bauer, M., & Pope, M. (2022). High-Resolution Estimation of Monthly Air Temperature from Joint Modeling of In Situ Measurements and Gridded Temperature Data. *Climate*, *10*(3), 47. https://doi.org/10.3390/cli10030047
Zhou, D., Zhao, S., Liu, S., Zhang, L., & Zhu, C. (2014). Surface urban heat island in China's 32 major cities: Spatial patterns and drivers. *Remote Sensing of Environment*, *152*, 51–61. https://doi.org/10.1016/j.rse.2014.05.017
Zhou, W., Huang, G., & Cadenasso, M. L. (2011). Does spatial configuration matter? Understanding the effects of land cover pattern on land surface temperature in urban landscapes. *Landscape and Urban Planning*, *102*(1), 54–63. https://doi.org/10.1016/j.landurbplan.2011.03.009
Zhu, W., Lű, A., & Jia, S. (2013). Estimation of daily maximum and minimum air temperature using MODIS land surface temperature products. *Remote Sensing of Environment*, *130*, 62–73. https://doi.org/10.1016/j.rse.2012.10.034